Asociación Argentina
de Mecánica Computacional

Mecánica Computacional Vol XXIX, págs. 3237-3255 (artículo completo)
Eduardo Dvorkin, Marcela Goldschmit, Mario Storti (Eds.)
Buenos Aires, Argentina, 15-18 Noviembre 2010

FLUID-STRUCTURE INTERACTION OF CYLINDERS BY COMBINING THE COSSERAT BEAMS THEORY AND IMMERSED BOUNDARY METHODOLOGY

Adailton S. Borges[a], João Marcelo Vedovoto[b], Felipe P. Mariano[b], Aristeu da Silveira Neto[b] and Domingos A. Rade[b]

[a]*Universidade Tecnológica Federal do Paraná - UTFPR, Departamento de Engenharia Mecânica, Av. Alberto Carazzai, 1640, Campus Cornélio Procópio, CEP 86300-000 - Cornélio Procópio - PR - Brasil, http://www.utfpr.edu.br/cornelioprocopio*

[b]*Universidade Federal de Uberlândia - UFU, Faculdade de Engenharia Mecânica - FEMEC, Av: João Naves de Ávila, 2121, Campus Santa Mônica, Bl:1M, CEP: 38400-902, Uberlândia-MG-Brasil, http://www.mecanica.ufu.br*

Keywords: Fluid Structure Interaction, Vortex Induced Vibration, Immersed Boundary Method, Cosserat Theory.

Abstract. A fully coupled simulation of three dimensional problems involving fluid structure interactions is the most accurate way to predict the behavior of high aspect ratio cylinders in cross flows. The main interest in this kind of flows are due the great number of applications in the oil and gas industry (especially the ones related to the modeling of risers used for oil exploitation in deep seas), however there are inherent difficulties in the simulation of the fluid structure interaction of long and thin cylinders, as example the high computational cost due the fact that a cylinder is moving across the computational domain associated with the necessity of the structural model be able to deal with high displacements. In this work we circumvent these difficulties by the joint of two methodologies: the combination of the Cosserat theory applied to slender beams, and the Immersed Boundary Methodology, which is used to represent the interactions between the structural and fluid domains. The main features of the proposed methodology are evaluated by means of a number of numerical simulations, both in static and dynamic regimes, regarding the structural model, in a first step and the complete fluid-structure model, in a second step. The results obtained permits to evaluate the accuracy and the main advantages and shortcomings of the methodology, especially regarding the numerical aspects. The results also, allow to put in evidence some relevant phenomenological aspects related to the dynamic behavior of cylindrical structures with various levels of bending flexibility, subjected to transverse flows characterized by different values of the Reynolds number.

1 INTRODUCTION

The flow past a cylindrical structure can be the source of vibrations generated by vortex shedding. Such vibrations can induce to an increase of the drag coefficient, thus leading to an increase of the efforts over structure. The vibrations can lead also to the failure of a structure due fatigue. This is especially important when these cylinders are risers of oil exploitation subject to waves and/or maritime currents. According to Baarholm et al. (2006), two approaches have been adopted for solving fluid-structure interactions (FSI): empirical models and methodologies based on numerical simulation of governing equations (for both fluid and structure).

The present work describes the research work carried-out with the aim of developing, implementing and evaluating a three-dimensional modeling procedure of fluid-structure phenomena involving slender structures, such as beams, bars and cables. The novel approach adopted consists in the combination of the Cosserat theory, Argyris et al. (1978), applied to slender beams, which accounts for geometrical nonlinearity, and the Immersed Boundary methodology, Lima e Silva et al. (2003), which is used to represent the interactions between the structural and fluid domains. The study is included in the scope of Vortex-Induced Vibrations, which is a topic of great interest in the oil industry. According to the Cosserat theory, the deformed configuration of the structure is described in terms of the displacement vector of the curved formed by the cross-sections center of area, and the orientation of a vector basis fixed to each cross-section, with respect to an inertial reference frame. The main advantage of this theory is that it is geometrically exact. The finite element method is employed for discretization of the equations of motion for the structure.

Through the Immersed Boundary methodology, the solid-fluid interface forces are evaluated by enforcing momentum to the fluid particles over the interface fluid-solid. Such a methodology is particularly suitable for problems involving fluid-structure interactions, once the difficulty of re-meshing the computational grid is circumvented by the use of two independent domains. The governing equations of fluid flow are solved in an Eulerian domain (fixed, cartesian for instance), while the immersed geometry (or geometries) is (are) represented by a set of Lagrangian points. The coupling between both domains is made by the utilization of interpolation/distribution functions, which are based on discrete versions of a Dirac delta function.

Regarding the structural model, its main features are evaluated by means of a number of numerical simulations in dynamic regimes in a first step and in a second step the complete fluid-structure model. The results obtained enable to evaluate the accuracy, and the main advantages and shortcomings of the methodology. They allow also to put in evidence some relevant phenomenological aspects related to the dynamic behavior of cylindrical structures with various levels of bending flexibility, subjected to transverse flows characterized by different values of the Reynolds number.

2 MATHEMATIC MODELING FOR FSI

The FSI numerical approach adopted is named partitioned, *i.e.* in the same time step (Δt) the coupling between the fluid and the structure is separated in two parts, first it is solved the transport and conservation equations of the fluid medium (Navier-Stokes equations), then the structure motion equations are solved by the Cosserat theory, as is shown in Fig. 1.

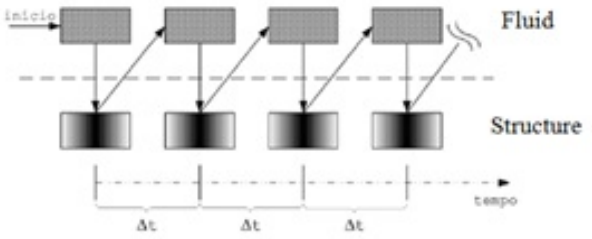

Figure 1: Partitioned approach for FSI.

The follow sections provide in details the formulation retained for the fluid, structure and the coupling between.

2.1 Mathematic model for the fluid

The flow is governed by momentum equation (Eq. 1) and the continuity equation (Eq. 2). The information of the fluid/solid interface (domain Γ) is passed to the eulerian domain (Ω) where a term source is added to momentum equations. This term plays a role of a body force that represents the boundary conditions of the immersed geometry. The equations that govern the problem are presented in their tensorial form:

$$\frac{\partial \rho u_i}{\partial t} + \frac{\partial (\rho u_i u_j)}{\partial x_j} = -\frac{\partial p}{\partial x_i} + \frac{\partial}{\partial x_j}\left[\mu\left(\frac{\partial u_i}{\partial x_j} + \frac{\partial u_j}{\partial x_i}\right)\right] + f_i, \tag{1}$$

$$\frac{\partial u_j}{\partial x_j} = 0. \tag{2}$$

where p is the static pressure; $u_i; i = 1, 2, 3$ are the velocity, f_i are the IB term source, ρ is the density, μ is the kinematic viscosity; x_i and t are the spatial component and the time, respectively.

The algorithm under consideration for the simulation of the fluid motion is based on a classical predictor-corrector time integration scheme that employs a projection method for the momentum equations. The finite volume spatial discretization of the Navier-Stokes equations (N-S equations henceforth) is based on a staggered framework with velocity and scalar quantities evaluated in different grids to avoid the rise of checkerboard pressure patterns.

Regarding the temporal integration of the N-S equations, the schemes retained are essentially controlled by the Courant criterion . Explicit schemes exhibit numerical stability issues when using Courant number values larger than unity. However, such a numerical limitation does not apply to implicit or semi-implicit discretizations. The temporal integration schemes retained in the present work are fully implicit, in such a manner that it is possible to reach statistically steady regimes faster than by resorting to explicit time integration techniques, Vedovoto (2009). To ensure robustness of a numerical method for solving the problems of interest, another important aspect analyzed in the present work is the choice of the temporal integration scheme. Here, besides the use of an fully implicit scheme permitting the use that allows to reach statistically steady regimes faster than by resorting to explicit time integration techniques, we adopt a formulation that allows the use of different methods of temporal integration, *e.g.* the Crank Nicolson method, a modified Crank Nicolson method, the Leap Frog and the backward difference formula methods.

The source term, f_i, defined in all domain Ω, is null, excepting the regions where the control volumes coincide with the immersed geometry, enabling the Eulerian field to perceive the presence of solid interface. Eq. 3 displays such a behavior.

$$f_i(\vec{x},t) = \begin{cases} F_i(\vec{x}_k,t) & \text{if } \vec{x} = \vec{x}_k \\ 0 & \text{if } \vec{x} \neq \vec{x}_k \end{cases} \tag{3}$$

Where $\vec{x}$ is the position of the particle in the fluid and $\vec{x_k}$ is the position of a point in solid interface, Mariano et al. (2010). Through Eq. 3 it is possible to conclude that the field $f_i(\vec{x},t)$ is discontinuous, and hence can be evaluated only when there is a coincidence between the points that compose the interface immersed boundary-fluid domain. It is rarely the case when there is a coincidence between the Lagrangian points and the control volumes. If a staggered framework of discretization is retained for the fluid equations, such a coincidence never happens once the primary variables of the fluid are positioned in different locations. When the flows of interest have complex geometries within the computational domain (Ω) it is necessary to distribute the function $f_i(\vec{x},t)$ on its neighborhoods. This is achieved by replacing the Dirac delta function by a discrete interpolation/distribution function. There are numerous forms of such a function. A detailed study of the form and efficiency of then can be found in Griffith and Peskin (2005).

2.2 Mathematic model for the immersed interface

The lagrangian force field is evaluated by the direct forcing methodology, which was proposed by Uhlmann (2005). One of the characteristics of this model is that ad-hoc constants are not necessary, therefore the modeling of non-slip condition on immersed interface is physically consistent. The Lagrangian force on the point k is evaluated by a balance of momentum over a particle of fluid coincident with the fluid-solid interface:

$$F_i\left(\vec{x}_k,t\right) = \frac{\partial \rho u_i}{\partial t}\left(\vec{x}_k,t\right) + \frac{\partial}{\partial x_j}\left(\rho u_i u_j\right)\left(\vec{x}_k,t\right) + \frac{\partial p}{\partial x_i}\left(\vec{x}_k,t\right) - \frac{\partial}{\partial x_j}\left[\mu\left(\frac{\partial u_i}{\partial x_j} + \frac{\partial u_j}{\partial x_i}\right)\right]\left(\vec{x}_k,t\right) \tag{4}$$

The values of $u_i(\vec{x}_k,t)$ and $p(\vec{x}_k,t)$ are provided by the interpolation of the respective velocities and pressure from the Eulerian field near the immersed interface. For the Lagrangian point $\vec{x}_k$ at the immersed boundary, one has:

$$F_i\left(\vec{X}_k,t\right) = \frac{u_i\left(\vec{x}_k,t+\Delta t\right) - u_i^*\left(\vec{x}_k,t\right) + u_i^*\left(\vec{x}_k,t\right) - u_i\left(\vec{x}_k,t\right)}{\Delta t} + RHS_i\left(\vec{x}_k,t\right), \tag{5}$$

where u^* is a temporary parameter, Wang et al. (2008), and $RHS_i(\vec{x}_k,t)$. Is the sum of the advective, pressure and diffusive contributions of Eq. 5. The latter equation is decomposed and solved by Eqs. 6 and 7 in same time step:

$$\frac{u_i^*\left(\vec{x}_k,t\right) - u_i\left(\vec{x}_k,t\right)}{\Delta t} + RHS_i\left(\vec{x}_k,t\right) = 0, \tag{6}$$

$$F_i\left(\vec{x}_k,t\right) = \frac{u\left(\vec{x}_k,t+\Delta t\right) - u_i^*\left(\vec{x}_k,t\right)}{\Delta t}, \tag{7}$$

where $u(\vec{x}_k,t+\Delta t) = U_{FI}$ is the immersed boundary velocity at the interface.

Equation 6 is solved on the Eulerian domain by the methods described in the section of mathematical and numerical methods for solving the fluid governing equations. u^* is interpolated

for Lagrangian domain, becoming u_i^* and it is computed on Eq. 7. Then the force F_i is smeared on the Eulerian grid. Finally, the velocity is updated by Eq. 8:

$$u_i\left(\vec{x}, t+\Delta t\right) = u_i^*\left(\vec{x}, t\right) + \Delta t.f_i. \tag{8}$$

2.3 Mathematic model for structure

2.3.1 Basic definitions and kinematic assumptions

One of the most important features of this theory is how the beam is spatially defined in terms of movement of the line passing through their cross sections centroids, defined by the vector $\mathbf{r}(s,t)$ in a Cartesian fixed (inertial) base represented by $F = \{\mathbf{e}_1, \mathbf{e}_2, \mathbf{e}_3\}$ with unit vectors e_i, and a set of orthogonal unit vectors attached to the cross section, forming the basis $S = \{\mathbf{d}_1(s,t), \mathbf{d}_2(s,t), \mathbf{d}_3(s,t)\}$, where the variable S represents the position of the cross section along the line of centroids. Therefore, for each point on the curve formed by the centroids there is a orthonormal moving frame, formed by the unit vector $\mathbf{d}_i(s,t)$, that are defined externally to the position vector $\mathbf{r}(s,t)$. In Fig. 2 shows a schematic representation of a segment of Cosserat beam, with the two vector basis mentioned above placed in it.

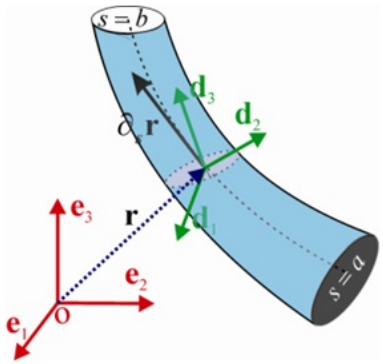

Figure 2: Schematic model of an element of Cosserat.

For convenience, $\mathbf{d}_1(s)$ and $\mathbf{d}_2(s)$ are adopted as contained in the plane of the cross-section and, as a consequence, the resulting $\mathbf{d}_3(s)$ is perpendicular to that plane. It is important to emphasize that such definition implies: a) in the condition of pure bending, the vector normal to the cross section, $\mathbf{d}_3(s)$, in each point of the curve of centroids, is coincident with the tangent of this curve, determined by the direction of the vector $\frac{\partial \mathbf{r}(s,t)}{\partial s} = \partial_S \mathbf{r}$; b) in the condition of pure shear, the same does not occur, in other words, the vector $\mathbf{d}_3(s)$ does not coincide with the direction of the spatial derivative the curve of centroids due to the distortion caused by shear. It is admitted, in both cases, that the cross section remains plane.

The line of centroids $\mathbf{r}(s,t)$ can be described in the inertial basis F as:

$$\mathbf{r}\left(s,t\right) = x\left(s,t\right)\mathbf{e}_1 + y\left(s,t\right)\mathbf{e}_2 + z\left(s,t\right)\mathbf{e}_3. \tag{9}$$

The strains can be defined as: linear deformations, denoted by $\mathbf{v}\left(s,t\right)$, and angular deformations, indicated by $\mathbf{u}\left(s,t\right)$. The linear deformations components $v_1\left(s,t\right)$ and $v_2\left(s,t\right)$ represent shear deformations, and the component $v_3\left(s,t\right)$ corresponds to elongation. In the same way, the components $u_1\left(s,t\right)$ and $u_2\left(s,t\right)$ represent the bending deformations, while the $u_3\left(s,t\right)$ component represents the torsion of the cross-section. As follows, those two classes of deformations will be defined.

In the first place, the linear deformation vector $\mathbf{v}(s,t)$, can be define from the variation of the centroids line along the s coordinate:

$$\mathbf{v}(s,t) = \frac{\partial \mathbf{r}(s,t)}{\partial s}. \tag{10}$$

In respect to the Eq. 10 it is important to emphasize that, due to the shear strain of the beam, the deformed cross section does not remains perpendicular to the line of centroids. However, for slender beams, the effect of shear can be neglected (Wang et al., 2004). Consequently, the element cross section is assumed to be perpendicular to the tangent of the centroids line, that is:

$$\mathbf{v}(s,t) = \frac{\partial \mathbf{r}(s,t)}{\partial s} = |\mathbf{r}'(s,t)|\,\mathbf{d}_3(s,t), \tag{11}$$

where the apostrophe indicates the derivative with respect to coordinate.

Hence, as demonstrated in Wang et al. (2004), the components of the normalized linear deformation are given by:

$$\mathbf{d}_3(s,t) = \frac{\frac{\partial \mathbf{r}(s,t)}{\partial s}}{|\mathbf{r}'(s,t)|} \triangleq v_1(s,t)\,\mathbf{e}_1 + v_2(s,t)\,\mathbf{e}_2 + v_3(s,t)\,\mathbf{e}_3. \tag{12}$$

In addition, it can be established the following relationship:

$$v_1^2(s,t) + v_2^2(s,t) + v_3^2(s,t) = 1. \tag{13}$$

Thus, the linear deformation can be written from Eq. 12 as follows:

$$v_1(s,t) = \frac{x'(s,t)}{|\mathbf{r}'(s,t)|}, \quad v_2(s,t) = \frac{y'(s,t)}{|\mathbf{r}'(s,t)|}, \quad v_3(s,t) = \frac{z'(s,t)}{|\mathbf{r}'(s,t)|}. \tag{14}$$

The vector of angular deformations $\mathbf{u}(s,t)$ is defined form the spatial derivative of the moving frame $\mathbf{d}_i(s,t)$:

$$\frac{\partial \mathbf{d}_i(s,t)}{\partial s} = \mathbf{u}(s,t) \times \mathbf{d}_i(s,t). \tag{15}$$

From Eq. 15 it is possible to find the following relationship (Cao et al., 2006):

$$\sum_{i=1}^{3}\left(\mathbf{d}_i \times \frac{\partial \mathbf{d}_i}{\partial s}\right) = \sum_{i=1}^{3}(\mathbf{d}_i \times (\mathbf{u} \times \mathbf{d}_i)) = \sum_{i=1}^{3}(\mathbf{u}(\mathbf{d}_i \cdot \mathbf{d}_i) - \mathbf{d}_i(\mathbf{d}_i \cdot \mathbf{u})) = 2\mathbf{u}. \tag{16}$$

By rearranging the Eq.16 it is possible to obtain the following expression:

$$\mathbf{u} = \sum_{i=1}^{3}\left(\frac{1}{2}\mathbf{d}_i \times \frac{\partial \mathbf{d}_i}{\partial s}\right). \tag{17}$$

In order to completely describe the kinematics of the Cosserat beam segment, besides the definition of the two classes of deformations acting on it, it is also necessary to determine the field of the cross sections rotations. Thus, the objective is to relate the components of the linear deformation vector with the rotation of the cross section. Such a procedure may be accomplished using two different parametrization methods. In literature, several parametrization

methods may be adopted for this end, among them, some may be listed: Euler angles; rotational vector (Euler's vector), quaternion parameters and Cayley transform, that can be found in Alamo (2006), Cao et al. (2006) and Rubin and Brand (2007). However, considering that the most usual are the Euler vectors and Euler angles, these methods were applied in this work, a better description can be found in Borges (2010). In the end of this procedure it is possible to establish a relationship between the rotation angles of the frame moving, $\varphi_x,\ \varphi_y\ e\ \varphi_z$ around the $\mathbf{e}_1,\ \mathbf{e}_2\ e\ \mathbf{e}_3$ axis respectively, and the torsion angle of the cross section ϕ and the linear deformation vector $\mathbf{v}$, given by:

$$v_1(s,t) = \frac{x'(s,t)}{|\mathbf{r}'(s,t)|} = \varphi_y(s,t) + \frac{1}{2}\varphi_x(s,t)\varphi_z(s,t) - \frac{1}{6}\left(\varphi_x^2(s,t) + \varphi_y^2(s,t) + \varphi_z^2(s,t)\right)\varphi_y(s,t), \tag{18}$$

$$v_2(s,t) = \frac{y'(s,t)}{|\mathbf{r}'(s,t)|} = -\varphi_x(s,t) + \frac{1}{2}\varphi_y(s,t)\varphi_z(s,t) + \frac{1}{6}\left(\varphi_x^2(s,t) + \varphi_y^2(s,t) + \varphi_z^2(s,t)\right)\varphi_x(s,t), \tag{19}$$

$$\phi(s,t) = \varphi_z(s,t) + \frac{1}{12}\left(\varphi_x^2(s,t) + \varphi_y^2(s,t)\right)\varphi_z(s,t). \tag{20}$$

It is necessary to emphasize that the Eqs. 19 - 20 will be of great importance to obtain the shape functions of the Cosserat beam element, for the finite element discretization purpose.

2.3.2 Equations of Movement

The local dynamic behavior of a beam element of Cosserat with density $\rho(s)$ and cross-sectional area $A(s)$, as shown by Antman (1995), is given by partial differential equations:

$$\frac{\partial \mathbf{h}(s,t)}{\partial t} = \frac{\partial \mathbf{m}(s,t)}{\partial s} + \mathbf{v}(s,t) \times \mathbf{n}(s,t) + \mathbf{l}(s,t), \tag{21}$$

$$\rho(s) A(s) \frac{\partial^2 \mathbf{r}(s,t)}{\partial t^2} = \frac{\partial \mathbf{n}(s,t)}{\partial s} + \mathbf{f}(s,t), \tag{22}$$

It is observed that Eqs. 21 - 22 are results of the application of the principles of Newton-Euler differential element of the beam. In these equations, $\mathbf{n}(s,t)$, $\mathbf{m}(s,t)$, $\mathbf{h}(s,t)$, $\mathbf{f}(s,t)$ and $\mathbf{I}(s,t)$ are respectively the contact force, the contact moment (internal), the angular momentum, the external force and external moment, all per unit of length.

One great concern associated to the finite element method is the choice of the shape functions. These functions are responsible for determining the displacement field inside the element from the nodal displacements. In the classic methods, they are usually approximated using low order polynomials. In the other hand, in the Cosserat beam theory, the shape functions can be obtained from the differential equations of static equilibrium, and so, they can take into account the system nonlinearities. Consequently, the precision of the dynamic response can be improved by dividing the structure in a few elements, which number is usually much lower than the amount required in the traditional finite element approach. However, the proceeds returned by using Cosserat theory are obtained in expense of a higher analytical and numeric complexity. The beam displacement functions, given in function of nodal displacements and rotations, are obtained from the solution of the equations of static equilibrium. Nevertheless, for the static

equilibrium, the equations of the movement become ordinary differential equations, where s is the only independent variable. In literature, the static equilibrium is understood as the absence of external forces, and from Eq. 21, the forces of contact must satisfy the expression:

$$\frac{d\mathbf{n}\left(s\right)}{ds}=0, \tag{23}$$

and, yet from Eq.22, the contact torque density satisfies:

$$\frac{d\mathbf{m}\left(s\right)}{ds}+\mathbf{v}\left(s\right)\times\mathbf{n}\left(s\right)=0. \tag{24}$$

Once defined the main vectors quantities involved in Eqs.23 - 24, it is necessary now to obtain the $m\left(s\right)$ and $n\left(s\right)$ in terms of deformations $\mathbf{u}\left(\mathbf{s}\right)$ and $\mathbf{v}\left(\mathbf{s}\right)$. That can be obtained from the constitutive relations of the material. It must be pointed that, in this work, it was used a constitutive model where the characteristics of a linear and elastic material were adopted, based on the constitutive relations of Kirchhoff (Cao et al., 2005). Thus, in this modeling it is assumed that Young Modulus E, the shear modulus G and the specific mass along the Cosserat beam element are only function of the spatial variable s, and the center of mass coincides with the centroid of the cross-section in s.

Therefore, using these relations, the forces and torque of contact are given as a function of linear and angular deformations, respectively (Borges, 2010) and, because of this, the Eqs.23 - 24 can be written in terms of the forces and contact momentum in the form of a highly nonlinear system given by:

$$n_1'\left(s\right)=u_3\left(s\right)n_2\left(s\right)-u_2\left(s\right)n_3\left(s\right), \tag{25}$$

$$n_2'\left(s\right)=u_1\left(s\right)n_3\left(s\right)-u_3\left(s\right)n_1\left(s\right), \tag{26}$$

$$n_3'\left(s\right)=u_2\left(s\right)n_1\left(s\right)-u_1\left(s\right)n_2\left(s\right), \tag{27}$$

$$m_3'\left(s\right)=u_2\left(s\right)m_1\left(s\right)-u_1\left(s\right)m_2\left(s\right). \tag{28}$$

In order to find the shape functions, it is necessary to solve the nonlinear system given by Eq. 25 - 28. It can be noted that those equations cannot be solved bay direct integration. Therefore, the perturbation method will be used in order to obtain an approximated solution. For this purpose, it was used a perturbation method oriented to this nature of solution and, among several available methods in literature, it was chosen the method of Frobenius (Arfken et al., 2000).

According to the Frobenius's method, the following approximations for the shape functions can be obtained:

$$x(s)=\bar{x}(\bar{s})L=\varepsilon x_1(s)+\varepsilon^2x_2(s)+\varepsilon^3x_3(s), \tag{29}$$

$$y(s)=\bar{y}(\bar{s})L=\varepsilon y_1(s)+\varepsilon^2y_2(s)+\varepsilon^3y_3(s), \tag{30}$$

$$z(s)=\bar{z}(\bar{s})L=s+\varepsilon z_1(s)+\varepsilon^2z_2(s)+\varepsilon^3z_3(s), \tag{31}$$

$$\phi(s) = \bar{\phi}(\bar{s})L = \varepsilon\phi_1(s) + \varepsilon^2\phi_2(s) + \varepsilon^3\phi_3(s). \tag{32}$$

The solutions presented here were obtained from a program of symbolic solution an due to the size of these solutions, they were intentionally omitted in this work, more information can be found in the work of Borges (2010).

It is important to emphasize that these displacement functions obtained with the from static equilibrium will later be used in the dynamic analysis, which eliminates on of the main problems usually found in the classic finite element theory, that is to define conveniently the shape functions.

2.3.3 Dynamic analysis by the finite element method

From the extended Hamilton's principle, it is possible to achieve the Lagrange equations, which constitutes a very elegant form to obtain the equations of movement of dynamic systems (Bathe, 2007). In this section, the equations of Lagrange are used to formulate the differential equations of movement of the Cosserat beam element.

The extended Hamilton principle is given by the following variational equation:

$$\delta \int_{t_1}^{t_2} (\mathrm{T} - \mathrm{V})dt + \int_{t_1}^{t_2} \delta W_{NC}^{F} dt = 0, \tag{33}$$

where T is the total kinetic energy of the system, V is the potential energy associated to the conservative forces and torque imposed, δ represents the variational operator and δW_{NC}^{F} is the work realized by the non conservative forces and torque imposed.

2.3.4 Kinetic and potential energies of the beam

Observing the Fig. 2 it is possible to note that the movement of the beam involves two types of velocities: the velocity of the centroids of the cross sections, $\frac{\partial \mathbf{r}(s,t)}{\partial t}$, and the angular velocities of the cross sections, $\omega(s,t)$. Therefore, the kinetic energy for unit of length is given by the following relation:

$$T^* = \frac{1}{2}\left[\frac{\partial \mathbf{r}(s,t)}{\partial t}\right]^T \rho(s) A(s) \frac{\partial \mathbf{r}(s,t)}{\partial t} + \frac{1}{2}\left[\omega(s,t)\right]^T \mathbf{I}(s)\,\omega(s,t), \tag{34}$$

where $\mathbf{I}(s)$ is the matrix of inertia of mass, in relation to a set of baricentric orthogonal axis.

In the other hand, considering small deformations, the elastic potential energy for unity of length can be expressed in terms of the deformations vectors $\mathbf{v}(s,t)$ and $\mathbf{u}(s,t)$ as follows:

$$U^* = \frac{1}{2}\left[\mathbf{v}(s,t)\right]^T \mathbf{K}(s)\,\mathbf{v}(s,t) + \frac{1}{2}\left[\mathbf{u}(s,t)\right]^T \mathbf{J}(s)\,\mathbf{u}(s,t) \tag{35}$$

given that $\mathbf{K}(s)$ e $\mathbf{J}(s)$ are determined by the association of the principal inertia of area of the cross section and the Kirchhoff constitutive relations for linear material. Thus, it is defined that J_1 and J_2 represents the shear stiffness and K_3 is the resistance to the elongation.

As can be noted, either the density of kinetic energy as the density of potential energy are functions of the variables time (t) and space (s). Hence, to find the discretized equations of movement, from the Hamilton principle and the equations of Lagrange, it is necessary to use the dimensional shape functions presented previously, Eq. 29 - 32. The complete description of

that procedure can be found in Borges (2010). In few words, the described procedure leads to the density of kinetic energy, Eq.34, and to the density of potential energy, Eq.35, as follows:

$$T^* = T^*\left(s, \dot{\mathbf{q}}^{(e)}(t)\right), \quad U^* = U^*\left(s, \mathbf{q}^{(e)}(t)\right), \tag{36}$$

where $\mathbf{q}^{(e)}$ represents the vector of generalized displacements for Cosserat beam element. So, the quantity known as lagrangian can be defined:

$$L\left(\mathbf{q}^{(e)}, \dot{\mathbf{q}}^{(e)}\right) = \mathrm{T}\left(\dot{\mathbf{q}}^{(e)}\right) - \mathrm{U}\left(\mathbf{q}^{(e)}\right) = \int_0^L \left[T^*\left(s, \dot{\mathbf{q}}^{(e)}\right) - U^*\left(s, \mathbf{q}^{(e)}\right)\right] ds \tag{37}$$

2.3.5 Virtual work realized by non conservative forces and momentum

At this moment, it is necessary to develop the term $\int_{t_1}^{t_2} \delta W_{NC}^F dt$ presented in Eq. 33 as a function of generalized coordinates. It is important to emphasize that this term is related to the virtual work performed by forces and torque non derivable from any potential function. It is assumed that the forces acting on the element are composed by three additive parts: the first one is proceeding from the interaction with surrounding elements; the second one is due to the action of external forces concentrated in nodal points; and, finally, the third one represents the external distributed forces with fixed directions and prescribed intensity. Therefore, the total virtual work realized by additive forces is given by:

$$\delta W_{NC}^F = \left(\mathbf{f}^{i(e)} + \mathbf{f}^{c(e)} + \mathbf{f}^{d(e)}\right)^T \cdot \delta \mathbf{q}^{(e)}, \tag{38}$$

where, $\mathbf{f}^{i(e)}$, $\mathbf{f}^{c(e)}$ e $\mathbf{f}^{d(e)}$ represent the internal forces and momentum, the external forces and momentum and, finally, the element distributed loading, respectively.

Substituting the Eqs. 37 and 38 in Eq. 33, using the chain rule and integrating by parts, it is obtained the equation of Lagrange for movement of a Cosserat element (Cao et al., 2006):

$$\frac{d}{dt}\left(\frac{\partial L}{\partial \dot{\mathbf{q}}_j^{(e)}}\right) - \frac{\partial L}{\partial \mathbf{q}_j^{(e)}} = \mathbf{f}_j^{i(e)} + \mathbf{f}_j^{c(e)} + \mathbf{f}_j^{d(e)}. \tag{39}$$

Performing some mathematical manipulations in Eq. 39 is possible to find the equations of movement with nonlinearities of same order of displacement functions, represented in Eq. 40. In the present study, such operations has been realized with the use of programs of symbolic manipulation.

$$\mathbf{M}^{(e)}\ddot{\mathbf{q}}^{(e)}(t) + \mathbf{K}^{(e)}\mathbf{q}^{(e)}(t) + \mathbf{g}^{(e)}\left(\mathbf{q}^{(e)}(t)\right) = \mathbf{f}^{i(e)}(t) + \mathbf{f}^{c(e)}(t) + \mathbf{f}^{d(e)}\left(t, \mathbf{q}^{(e)}\right), \tag{40}$$

where $\mathbf{M}^{(e)}$ is the element mass (linear), $\mathbf{K}^{(e)}$ is the linear stiffness matrix, $\mathbf{g}^{(e)}\left(\mathbf{q}^{(e)}\right)$ is the non-linear vector which contains the quadratic and cubic terms of $\mathbf{q}^{(e)}$.

Once determined the matrix of mass, stiffness and nodal equivalent forces for each Cosserat beam element, the mechanical connection among the different elements should be established, which is performed by the process of assembling of global equations of movement for the system. Such a procedure is a standard in finite element modeling, so, they will not be presented the present work.

It is important to emphasize that those set of equations are highly nonlinear and require the use of robust integrator in order to determine the displacement and velocity fields, whose will be approached later. As presented by Borges (2010), several solution methods were tested, such as Newmark with imposed conservation of mechanical energy, proposed by Bathe (2007); the Newmark method combined with the Newton-Raphson algorithm, suggested by Géradin and Rixen (2001); and the Runge-Kutta of forth order method with variable step. The most efficient and robust was the Newmark with imposed conservation of mechanical energy, so, it was retained in all simulated cases.

2.4 Fluid-structure interaction

This section defines the methodology used to coupled the fluid and structural domains. Note that the mesh in these two domains are different, as illustrated in Fig. 4, which states that the surface mesh of the immersed body is composed by rectangular elements; the discretization of the structural domain, according to the theory of Cosserat, is formed by nodes positioned about a central line.
A major issue faced in this stage is how to transfer forces and moments applied by the fluid on the surface of the cylinder, calculated by immersed boundary method, to the nodes of the mesh structure, and backwards, from the structure to the finite element nodes, thus transferring the displacements, velocities and accelerations are calculated using the theory of Cosserat beam to the surface of the cylinder that will be in contact with the fluid.

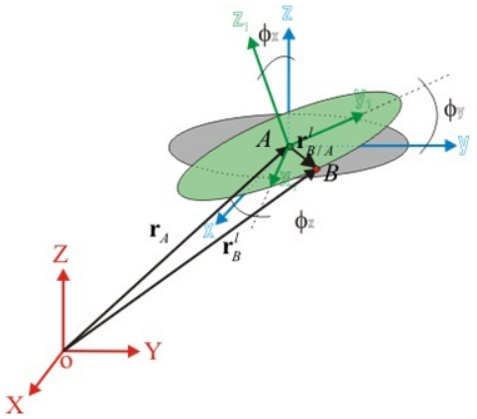

Figure 3: Sketch of cylinder slice and reference axes.

The procedure adopted is to consider "slices" of the cylindrical surface mesh in the direction "z" composing a row of elements and attach it to a given nodal point of the mesh structure, so that the forces as well as the moments applied on the node of the structure mesh, are the result of demands imposed on all nodes in the mesh of fluid on the surface of the "slice" of the cylinder. In Fig. 4, the red point represents the Lagrangian point of the immersed structure and the green point represents the node of the mesh structure. To accomplish the transfer of information between the two domains becomes necessary to use auxiliary axis of references. In this modeling were used three axes, which are shown in Fig. 3, two of them mobile $(Axyz)$ and $(Ax_1y_1z_1)$ and a fixed $(OXYZ)$. Thus using the concepts of kinematics and dynamics of three-dimensional motion of a rigid body, forces and moments can be transferred from the surface of the cylinder immersed into the structure nodal point, and in reverse, transferring

the displacement and velocity of the structural nodal point to surface immersed. Note that the solution algorithm for the fluid-structure coupling is made using a partitioned method, thus solving one of the domains separately, and then using its results as input in subsequent domain.

The Cosserat theory beans is coupled with immersed boundary method to obtain the structural dynamic reaction support by excitation forced for the flow. For understand the fluid-structure interaction using the partitioned algorithm it is proposed the following steps:

1. Transport Eulerian equations of momentum are solved (Eq. 6), yielding the temporary parameter (u_i^*);
2. The temporary parameter (u_i^*) is interpolated to the Lagrangian domain;
3. The Lagrangian force, $F(\vec{x}_k, t)$ is evaluated (Eq. 7). It is noteworthy that in this case the velocity U_{FI} is the structure velocity given also by the Cosserat theory;
4. As commented before, the displacements, velocity and acceleration of the structure are evaluated over a line positioned at the centroid of the immersed body, therefore it is necessary to evaluate the sum of the Lagrangian forces, $\sum_{nl} F(\vec{x}_k, t)$ and torque, $\sum_{nl} \vec{T} = \vec{r} \times \vec{F}$, (being $\vec{r}$ is the distance between lagrangian point and a node of structure center line) at such a line (Fig. 4) exemplifies this procedure;

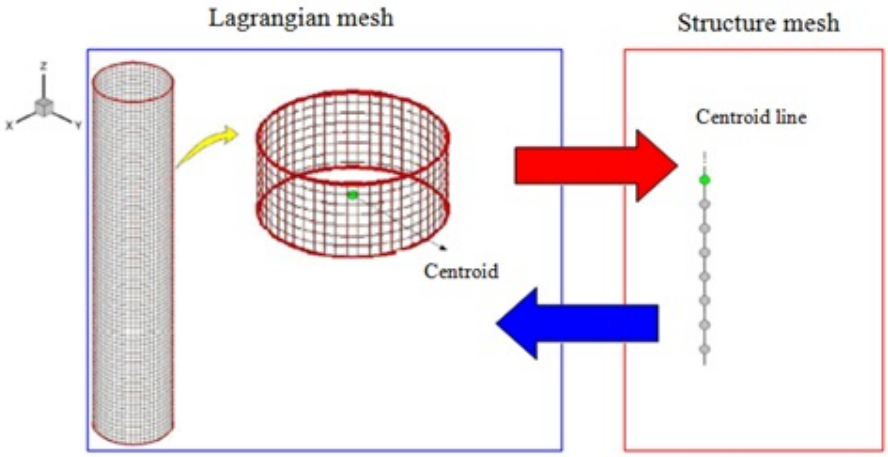

Figure 4: Coupling between the fluid and structural meshes.

5. The force evaluated at each Lagrangian point if $F_i(\vec{x}_k, t)$ smeared over the Eulerian domain, yielding the Eulerian force, $f_i(\vec{x}, t)$;
6. The Eulerian velocity field is updated (Eq. 8);
7. The Poisson equation is solved and the velocity field is updated with the pressure correction, finalizing the pressure-velocity coupling;
8. The sum of the Lagrangian forces and torque (calculated in forth step) is evaluated and a new position and velocity of center line structure, consequently the new positions of the Lagrangian points, are given;
9. Return to step (1).

3 RESULTS

3.1 Structural methodology evaluation and validation

An initial requirement to envisage simulating fluid structure problem is to validate the numerical methods implemented in canonical tests. In this section we validate the structural modulus in a dynamic regime. One of the main difficulties in simulating nonlinear structures in dynamic regime is to find an integrator sufficiently precise and stable for long simulation periods of time. Hence, the test structure was also used for validation of the integration method adopted. The tested structure, which will be used for validating the numeric algorithm presented here, is the free cantilever beam illustrated in Fig. 5.

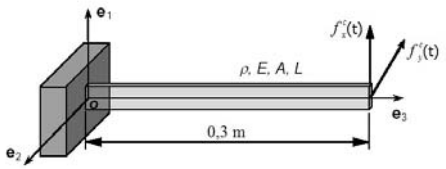

Figure 5: Testing structure.

This model, was firstly implemented by Cao et al. (2005), with the following dimensions: $0.3\ m$ of length, cross section of 0.01 m of width and 0.05 m of thickness. The values of Young modulus and density adopted were $2.0810^8\ Pa$ e $3.0010^3\ kg/m$, respectively. The excitation forces in x and y directions were $f_x^c(t) = 0,01\cos(8t)$ and $f_y^c(t) = 0,005\sin(8t)$, applied in free end of the beam. It must be pointed that in the work presented by Cao et al. (2005) the testing structure was evaluated using Cosserat beam element obtained from third order approximation of shape functions. The same approach is used to validate the methodology proposed in the present work.

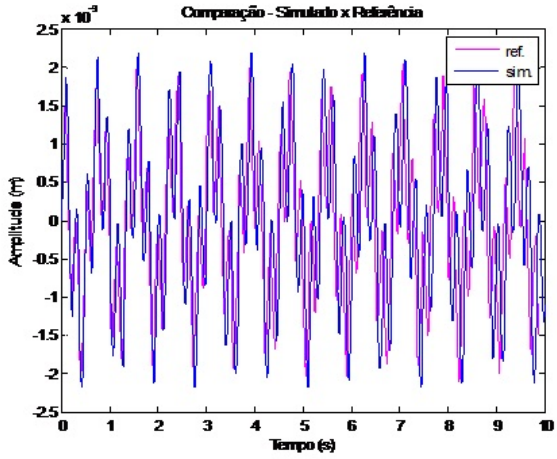

Figure 6: Comparison between structure displacement in x direction. (ref: presented by Cao et al. (2005); sim: present work).

Figure 6 presents the displacements obtained for the free end of the beam in x direction, with the corresponding values obtained by Cao et al. (2005). In the same way, the Fig. 7 shows a

comparison between the results obtained in y direction. Both methods discretized the structure in 10 equally spaced elements. The integration method used was the Newmark with imposed conservation of mechanical energy, suggested by Bathe (2007), and the step used was 0.01 s.

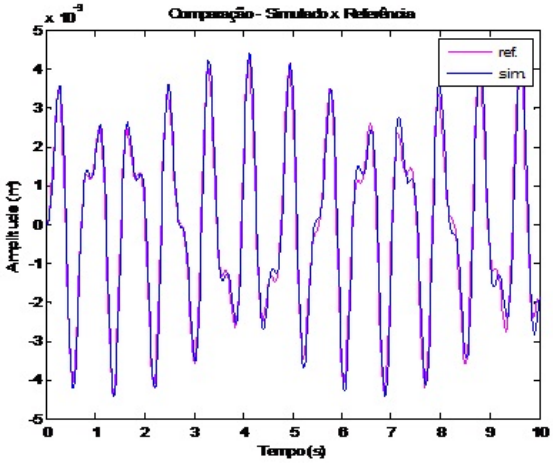

Figure 7: Comparison between structure displacement in y direction. (ref: presented by Cao et al. (2005); sim: present work).

Observing Figs. 6 and 7 is possible to note small differences between the two sets of results, which can be due to the using of different methods of numeric integration for the equations of the movement. However, as the deviations found were negligible, the implementation of the Cosserat beam theory can be considered validated.

3.2 Fluid Methodology evaluation and validation

In this section we present the results of the simulations carried out for both validation of the numerical code, and of the simulation of flexible structures subject to cross flow. The effects of different Reynolds numbers ($Re = \rho U D/\mu$, where U is the uniform velocity imposed inlet and D is diameter of cylinder) are assessed. The eulerian domain has dimensions $30x20x10$ in directions X, Y and Z, respectively, the base of cylinder is positioned in $10x10x0$, in relation to coordinate axes $OXYZ$. For all simulations carried in this work the cylinder has a diameter $D = 1.0$ and a length $L = 10.0$, as show in Fig. 8.

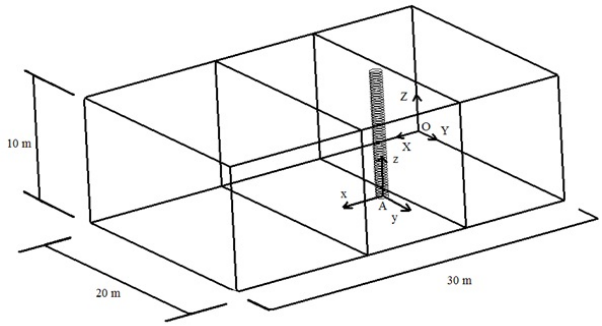

Figure 8: Eulerian and lagrangian domains.

The boundary conditions for the Eulerian domain flow in the plane $X = 0$ is a uniform inlet profile $U = 1.0$ [m/s] and at plane $X = 30$ the advective boundary condition is imposed. For

other boundary conditions (planes $Y = 0$, $Y = 20$, $Z = 0$ and $Z = 10$) no-slip boundary conditions is imposed. All simulations used a cartesian uniform mesh divided in three parallels sub domains, Vedovoto (2009).

3.3 Rigid structure

In order to validate the flow solver, the first simulations are performed without move the cylinder *i.e.* $EI = \infty$ at different Reynolds numbers. Drag (Cd) coefficient and Strouhal numbers (St) are compared with the data provided by White (1991) and shown in Tab. 1. The differences between Strouhal number present in Tab. 1 is probably due the proximity of boundary conditions of the cylinder and the length of cylinder.

	Re=100		Re=500		Re=1000	
Authors	Cd	St	Cd	St	Cd	St
White (1991)	1.40	0.18	1.30	0.21	1.10	0.21
Present work	1.51	0.14	1.31	0.16	1.30	0.16

Table 1: Comparison among different Reynolds numbers for drag coefficient and Strouhal number.

3.4 Flexible structure

The flexible structure is modeled by the Cosserat theory for slender beams. The hydrodynamic forces required by such a methodology are provided by the immersed boundary method. Three different values of Reynolds number were studied ($Re = 100$, 500 and 1000). The physical and geometrical properties of the flexible cylinder are given in Tab. 2.

Properties	Values
Aspect ratio (L/D)	10
Density	7850 [Kg/m^3]
Axial stiffness(EA)	501.39 [N]
Bending stiffness(EI)	9.07 [Nm^2]
Torsion stiffness (GJ)	6.82 [Nm^2/rad]

Table 2: Physical and geometrical properties of the flexible cylinder.

As boundary conditions for the structure model, revolute joints are adopted and hence displacements both the extremities and the torsional degrees-of-freedom were eliminated, allowing however, rotation in the directions x and y. The immersed structure is discretized using 50 Cosserat elements equally spaced, with 51 nodes and 6 degrees of freedom by node.

Figure 9 displays the temporal evolution of the flow past a flexible cylinder at different times at $Re = 1000$. Due to structural stiffness, and the magnitude of hydrodynamic forces imposed by flow, was observed a deformation of the structure. It is observed in Fig. 9 the Von Karman wake, characterized by the periodic vortex shedding (which is responsible for exciting the structure in the direction transverse to the flow). It is notable the deformation of the structure and its effects in the fluid wake. The shedding of the coherent fluid structures are affected in the sense that when the structure moves towards the flow there is a decreasing in the number of vortex liberated, the opposite effect is present when the structure tries to recuperate its initial form and goes against the flow. In this case it is possible to note a higher number of coherent structures.

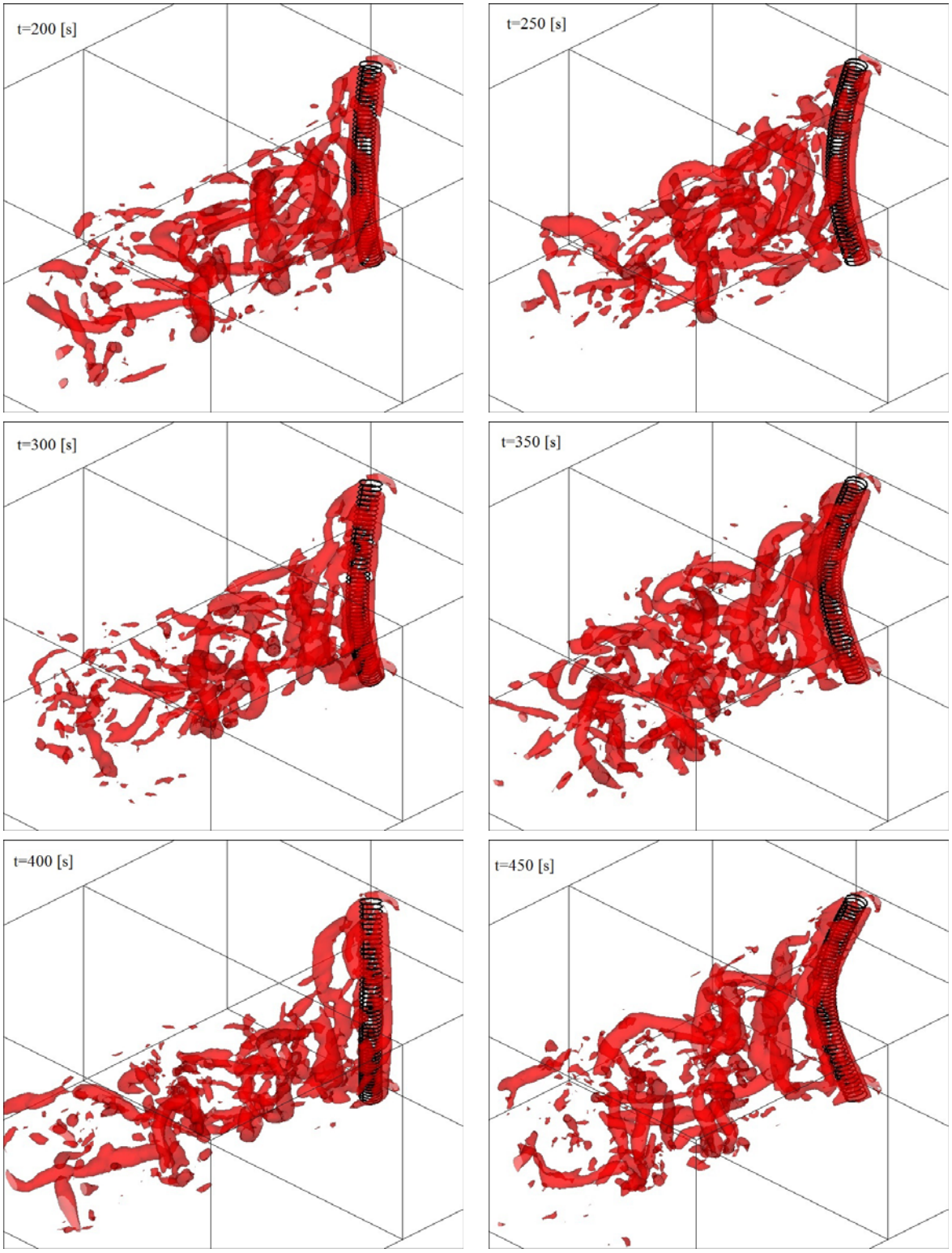

Figure 9: Temporal evolution de isosurface of ($Q = 0.25$) at $Re = 1000$.

For a quantitative evaluation of the flows here simulated Fig. 10 shows the drag and lift coefficients for simulations at different Reynolds numbers. Even tough for the simulations at $Re = 100$, there is not a great difference in the wake, the vibration of the cylinder is sufficient to alter the patterns of the drag and lift coefficients. Such a phenomena is intensified as the

Reynolds number increases.

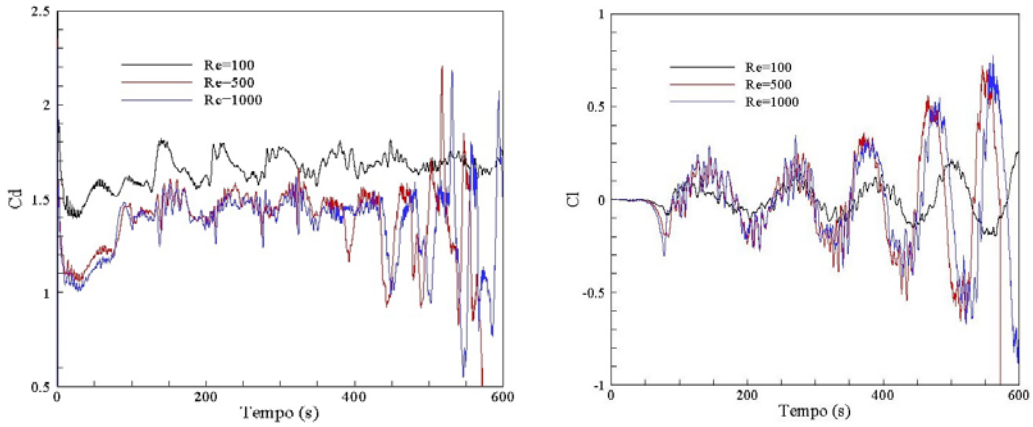

Figure 10: Temporal evolution of drag and lift coefficients at different Reynolds Numbers.

In Fig. 10 is noteworthy the effect of the Reynolds number in the quantitative coefficients. Since a higher Reynolds number implies in higher efforts over the structure is natural an increase in the values of displacements of the flexible body. This phenomena promotes thus a higher oscillation of the signals, especially for Reynolds number higher than 500.

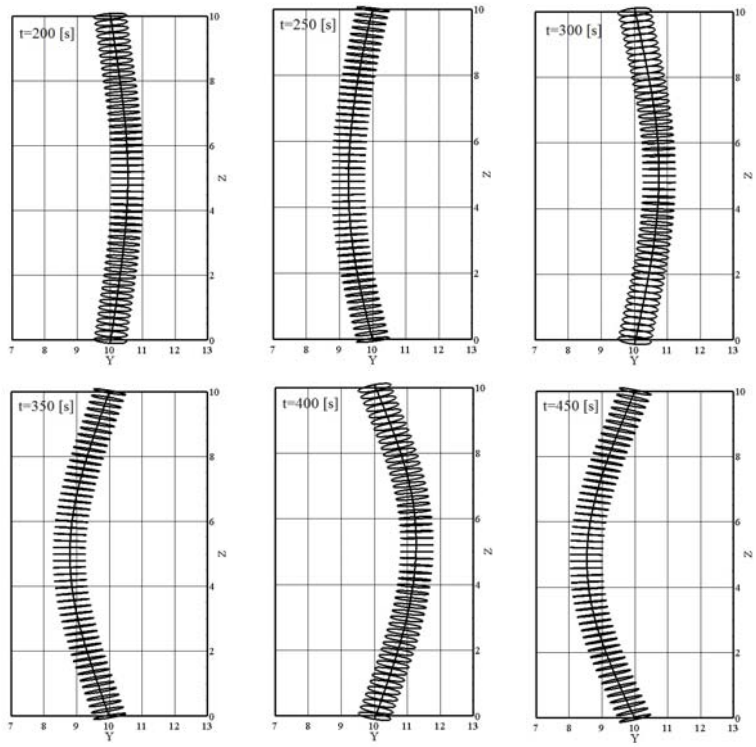

Figure 11: Instantaneous position of the immersed structure at $Re = 1000$.

In order to demonstrate the real dimension of the structure displacement Fig. 11 demonstrate that at Reynolds 1000 the lateral deformation of the structure achieves 20% of the total length. At $t = 450[s]$ for example, it is possible to note that the lateral displacement achieves 2 m in Y direction near the half length of the cylinder.

It is important to point-out that only the immersed boundary and structural meshes are shifted. The Eulerian cartesian grid stands still, so even with great deformations the computational cost associated with the simulations remains

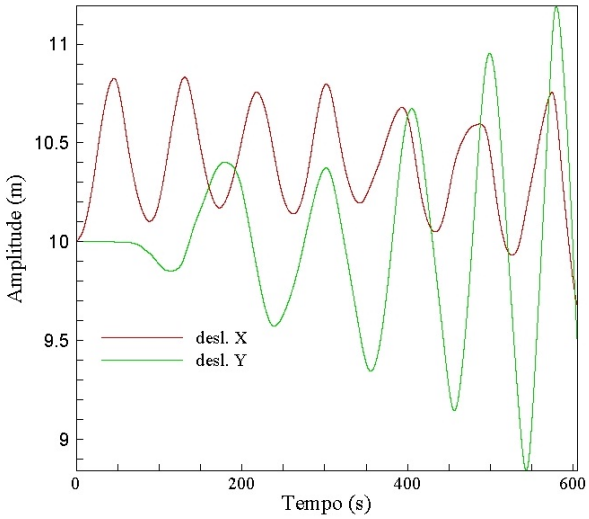

Figure 12: Displacement of a point positioned at the central line of the cylinder at z=5 [m]; Re=1000.

In Fig. 12 one notices the differences between the structural shifts in the longitudinal and transverse direction. Due to the complexes patterns of deformation of the structure, and its low stiffness, the computational showed itself insufficient for the simulation at Reynolds 1000. However, the magnitude of the displacements which the immersed geometry is subject demonstrate the capacity of the Cosserat theory in dealing with the great shifts imposed by the hydrodynamic forces.

4 CONCLUSIONS

We present a new approach for FSI problems applied to flexible cylinders. This promising approach is better detailed in work of Borges (2010) and Vedovoto (2009), allowing to solve problems with large deformations. It is a major area of interest of the oil industry. The Cosserat theory and immersed boundary method enabled to simulate a full FSI problem, which the structure movement is produced just by fluid flow forces. While all characteristics of flow, laminar or turbulent, are preserved. New simulations are been performed to obtain large aspect ratios, for this aspects as code parallelism are being implemented.

5 ACKNOWLEDGEMENTS

The authors thank the College of Engineering Mechanical ($FEMEC$) of the University Federal of Uberlândia (UFU), $Capes$, $FAPEMIG$ and $CNPq$ for financial support.

REFERENCES

Alamo F. Dinâmica de estruturas unidimensionais esbeltas utilizando o contínuo de cosserat. *Tese de doutorado-Departamento de Engenharia Mecânica - Pontifícia Universidade Católica do Rio de Janeiro*, 2006.

Antman S. Nonlinear problems of elasticity. *Applied Mathematical Sciences*, 2:884–885, 1995.

Arfken G., Weber H., and Harris F. *Mathematical Methods for Physicists*, volume 5. Academic Press Inc., 2000.

Argyris J., Dunne P., Malejannakis G., and Scharpf D. On large displacements-small strain analysis of structures with rotational degree of freedom. *Computer Methods in Applied Mechanics and Engineering*, 14:99–135, 1978.

Baarholm G., Larsen C., and Lie H. On fatigue damage accumulation from in-line and cross-flow vortex-induced vibrations on risers. *Journal of Fluids and Structures*, 22:109–127, 2006.

Bathe K. Conserving energy and momentum in nonlinear dynamics: A simple implicit time integration scheme. *Computers and Structures*, 85:437–445, 2007.

Borges A. *Desenvolvimento de procedimentos de modelagem de interação fluido- estrutura combinando a teoria de vigas de Cosserat e a metodologia de fronteira imersa*. Universidade Federal de Uberândia - PhD. These, 2010.

Cao D., Dongsheng L., Charles H., and Wang T. Nonlinear dynamic modelling for mems components via the cosserat rod element approach. *J. Micromech. Microeng*, 15:1334–1343, 2005.

Cao D., Dongsheng L., Charles H., and Wang T. Three dimensional nonlinear dynamics of slender structures: Cosserat rod element approach. *International Journal of Solids and Structures*, 43:760–783, 2006.

Géradin M. and Rixen D. *Theory and application to structural dynamics*, volume 2. John Wiley and Sons, 2001.

Griffith B. and Peskin C. On the order of accuracy of the immersed boundary method: higher order convergence rates for sufficiently smooth problems. *Journal Computational Physics*, 208:75–105, 2005.

Lima e Silva A., Silveira-Neto A., and Damasceno J. Numerical simulation of two dimensional flows over a circular cylinder using the immersed boundary method. *Journal of Computational Physics*, 189:351–370, 2003.

Mariano F., Moreira L., Silveira-Neto A., da Silva C., and Pereira J. A new incompressible navier-stokes solver combining fourier pseudo-spectral and immersed boundary method. *Computer Modeling in Engineering Science*, 59:181–216, 2010.

Rubin M. and Brand M. A constrained theory of a cosserat point for the numerical solution of dynamic problems of non-linear elastic rods with rigid cross-sections. *International Journal of Non-Linear Mechanics*, 42:216–232, 2007.

Uhlmann M. An immersed boundary method with direct forcing for the simulation of particulate flows. *Journal of Computational Physics*, 209:448–476, 2005.

Vedovoto J. *Desenvolvimento de uma modelagem da combustão em escoamento turbulento baseada em metodologia híbrida euleriana/lagrangiana e na metodologia da fronteira imersa*. Universidade Federal de Uberândia - Relatório de qualificação, 2009.

Wang C., Liu D., Rosing R., Richardson A., and De Masi B. Construction of nonlinear dynamic mems component models using cosserat theory. *Analog Integrated Circuits and Signal Processing*, 40:117–130, 2004.

Wang Z., Fan J., and Luo K. Combined multi-direct forcing and immersed boundary method for simulating flows with moving particles. *International Journal of Multiphase Flow*, 34:283–302, 2008.

White F. *Viscous fluid flow*, volume II. McGraw Hill, 1991.